Contrib Mineral Petrol (1995) 120: 412–425

Nelia W. Dunbar · Gary K. Jacobs · Michael T. Naney

Crystallization processes in an artificial magma: variations in crystal shape, growth rate and composition with melt cooling history

Received: 27 May 1994/Accepted: 5 December 1994

Abstract A large (4.8 m^3, 1.3×10^7 g) artificial mafic melt with a bulk composition similar to that of a basalt (but with a high CaO content of 17 wt %) was generated during a demonstration of in situ vitrification and was allowed to cool naturally. During the melting process, convection was vigorous, resulting in a chemically and thermally homogeneous melt body. Once heating was complete, the cooling rate was rapid with the temperature dropping from 1500° C to 500° C in ~6 days within the interior of the 3 m diameter, 1.5 m thick body. A ~20 h period of constant temperature (1140° C) observed during cooling was the result of latent heat released by widespread crystallization. The final crystalline assemblage consists of diopsidic to hedenbergitic pyroxene and anorthitic feldspar, with a subordinate amount of potassic feldspar, plus a small amount of evolved glass. The compositions and proportions of phases agree well with those predicted by the MELTS thermodynamic model. Thermal and textural evidence suggest that convection within the melt ceased coincident with formation of the first crystals. Textural investigation of core samples reveals large (up to 1 cm in length) acicular diopsidic pyroxenes in a matrix of smaller feldspar and zoned pyroxene crystals (~500 μm in length). Crystal shape and pyroxene composition vary as a function of position within the solidified body, as a function of cooling rate. Both crystal size and degree of crystallinity are highest in the central, most slowly-cooled parts of the rock. Crystal shape is characterized by tabular, equilibrium-growth forms in the slowly-cooled areas, grading to highly skeletal, dendritic forms at the rapidly-cooled edges of the body. The pyroxene crystals are dominantly homogeneous diopside, but crystals are characterized by thin Fe-rich hedenbergitic rims. These rims were deposited when Mg in the melt was depleted by diopside growth, and melt temperature had cooled sufficiently to allow Fe-rich pyroxene growth. Crystal growth rates can be calculated based on thermal behavior of the melt, reinforced by thermodynamic modelling, and are determined to be between 10^{-7} and 10^{-8} cm/s in the central part of the melt. These estimates agree well with growth rates in natural systems with similar cooling rates. Pyroxene crystals that formed at a higher cooling rates are characterized by higher Al and lower Mg contents relative to tabular equilibrium crystalline forms, presumably as a result of disequilibrium melt compositions at the crystal-melt interface.

N.W. Dunbar (✉) · G.K. Jacobs · M.T. Naney
Environmental Science Division, Oak Ridge National Laboratory, Oak Ridge, TN, 37831 USA

Current address
[1] New Mexico Bureau of Mines and Mineral Resources, New Mexico Institute of Mining and Technology, Socorro, NM 87801, USA

Editorial responsibility: T.L. Grove

Introduction

Crystallization is a process that drives the evolution of magmatic systems. Crystal shape and growth rates within magmatic systems are controlled by latent heats of fusion, diffusion of chemical components within the melt, reactions at the crystal-melt interface, and degree of undercooling of the system (e.g., Kirkpatrick 1976; Lofgren 1980; Swanson and Fenn 1986). The kinetics of nucleation also affect crystallization processes, possibly influencing the distribution of crystals within a magma body (e.g., Lofgren 1983; Brandeis et al. 1984). Studies of crystal sizes in well-constrained natural systems suggest that crystal nucleation and growth rates decrease with increasing crystallinity of the melt, and that crystallization can begin at small degrees of undercooling (Cashman and Marsh 1988). Once crystal growth is initiated, the shape of the crystal is strongly dependent on growth rate, which is, in turn, dependent on the cooling rate and degree of undercooling during growth (Lofgren 1980). Continuous cooling rate experiments

have been useful for determining cooling regimes in natural systems (Lofgren 1980). However, in experimental systems it is difficult to simulate the effect of latent heat release by crystallization in the thermal regime of a large magma body, and thus latent heat effects are generally ignored (e.g., Lange et al. 1991).

Chemical processes that take place at the crystal-melt interface are also important. If some components diffuse away from the crystal-melt interface at rates slower than crystal growth, a chemically altered zone will be produced around the crystal and the crystal can become inversely chemically zoned with respect to slower diffusing components (Albarede and Bottinga 1972). This behavior will result in growth of crystals which are not in equilibrium with their parent melt, and may also lead to skeletal growth shapes (Lofgren 1980). This effect may also lead to crystals of different composition growing from a single composition parent melt, simply due to the crystal growth rate (Grove and Bence 1977). Crystals that grow rapidly may be homogeneous, but may be relatively more enriched in elements that are less compatible in the crystalline structure because of enrichment of these elements at the crystal-melt interface. Without considering cooling rate, such differences in mineral composition might be interpreted as a result of crystallization from different magmatic compositions.

Investigations of crystallization in laboratory experiments and well-constrained natural systems have proven useful for understanding complex crystallization processes. An artificial melt produced at Oak Ridge National Laboratory (ORNL) provided a unique opportunity to investigate crystallization processes in an unusually large artificial system. During cooling, the hemispheric-shaped melt crystallized to an assemblage similar to that observed in some mafic igneous rocks. The degree and characteristics of crystallization vary with distance from the central part of the melt. The melt was large enough to permit processes occurring in natural systems to operate (e.g., convection and crystal-liquid fractionation, Jacobs et al. 1992; Dunbar et al. 1993), yet allowed many aspects of control and monitoring typical of a laboratory experiment (temperature monitoring, chemical and physical characterization before and after the test). Information derived from study of this melt provides insight into physical and chemical process of magmatic crystallization.

Background on ISV

In situ vitrification (ISV) is a technique developed to stabilize hazardous and radioactive waste sites through resistance (joule) heating and melting of contaminated soil (Buelt et al. 1987; Jacobs et al. 1992). ISV was developed and patented by Battelle's Pacific Northwest Laboratory for the United States Department of Energy. Graphite electrodes, each up to 0.3 m in diameter are placed vertically at ground level over the area to be melted. Resistance heating occurs as electrical current is applied to the ground via the electrodes, and melting proceeds downward and outward producing a roughly hemispheric body. Spacing between the electrodes can be up to 5 m, and up to 9×10^8 g of soil have been melted in the largest ISV tests (J. Tixier, personal communication, 1992). A hood, maintained at slightly below atmospheric pressure, covers the molten zone, collecting and filtering all gases and particles released from the melt surface. The upper surface of the melt body subsides during melting due to pore space loss and resultant volume decrease that occurs when soil is melted. Figure 1 schematically illustrates the ISV equipment and some characteristics of a test conducted at ORNL.

The purpose of the ISV test conducted at ORNL during May, 1991 was to evaluate the feasibility of ISV for stabilizing trenches used at ORNL from 1951 to 1966 to dispose of liquid radioactive wastes. The test area was constructed in a saprolite of the Maryville formation (interbedded shale and limestone). A pit was excavated so that a scale-model of an actual disposal trench could be constructed and instrumented. The scale-model trench, filled with dolomitic limestone gravel, was 1.2 m high, 1.8 m long, with a width of 1 m at its top and 0.3 m at its bottom. The volume around the trench was backfilled with the native soil. An array of sensors was placed in and around the test trench to monitor temperature, pressure and heat

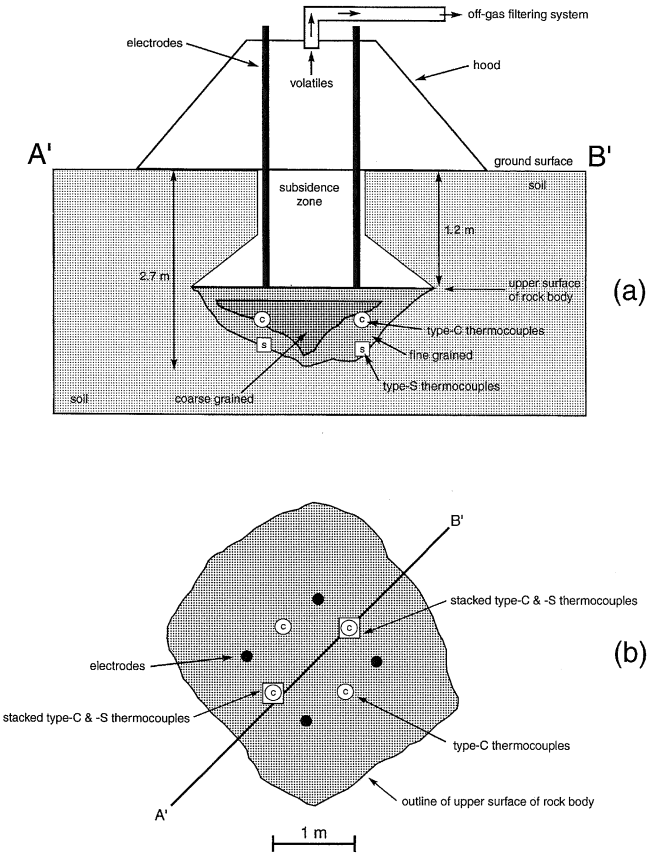

Fig. 1a Cartoon of general ISV site, showing electrode configuration, general melt shape, subsidence zone and hood. The approximate shape of ISV melt as determined by cores drilled through the cooled body, is shown. The *darker area* in the central portion of the melt shape represents a boundary in physical characteristics of the rock, distinguishing the central area of highest crystallinity versus the less-crystalline outer rim. Location of the type-C (near melt core) thermocouples is shown. **b** Map view of the ISV melt showing the spatial distribution of type-C and type-S thermocouples

flux during the melting process. The final melt included approximately 80% soil and 20% dolomitic limestone. Known quantities of three non-volatile tracers La_2O_3 (1510 g), Nd_2O_3 (1008 g), and CeO_2 (1509 g) were placed as point sources along a vertical profile in the center of the volume to be melted. Concentrations of these tracers in the final rock were measured and used to determine the final mass of the rock body (by dilution of known initial inputs of these tracers) and the effectiveness of convection in homogenizing the concentrations of the tracers.

Melting was initiated at the surface, and continued for 127.5 h, using a total of 29 MWh of electrical power. Observations of the melt surface were made during active melting. When visible, the surface glowed bright orange, resembling the molten surface of a Hawaiian lava lake. Slight bubbling and active convection with rates estimated at $\sim$0.1 m/s (visual estimation) were visible on the molten surface. The vigorous convection suggested that the melt was being effectively mixed, but the number and configuration of convective cells could not be accurately determined.

Thermal monitoring

The temperature of the melt and surrounding soil was monitored with 93 thermal sensors placed in and around the test trench. These sensors included 73 type-K (chromel vs alumel thermocouples), 12 type-C (W-5%Re vs W-26%Re thermocouples) and 2 type-S (Pt vs Pt-10%Rh thermocouples). The type-K thermocouples burnt out and ceased to function shortly after being contacted by the melt, and were used to monitor the size of the molten body. The type-C and type-S thermocouples protected by alumina thermal wells and optical pyrometers could withstand melt temperatures, and were used to monitor temperature in the molten body during the melting and cooling periods. Six protected thermocouples were able to record the thermal history of melt generation and solidification. The four type-C that recorded melt temperatures were each located 90° apart in a horizontal plane about half-way down the melt body (Fig. 1). Each was located approximately 0.7 m from the central axis of the melt. The two type-S thermocouples were about 0.5 m below the type-C thermocouples, so were close to the base of the melt. Temperature measurements for each sensor were recorded every 4 min during heating, active melting and cooling. Temperature uncertainty is estimated to be $\pm$ 20° C.

Sample collection and preparation

When the melt had cooled to ambient temperature, 17 drill cores were obtained from the rock body, and samples for observation and geochemical analysis were taken from these cores. Samples for whole rock analysis were crushed and then ground in agate. Polished sections for petrographic observation and microbeam geochemical analysis were made from core samples mounted in epoxy on 1″ round glass slides and then ground and polished with pure diamond grit suspended in distilled water.

Whole rock analysis

Whole rock composition (major and trace elements) were analyzed by x-ray fluorescence (XRF) and neutron activation analysis (NAA), both at New Mexico Institute of Mining and Technology. XRF determinations of major elements and trace elements Rb, Sr, Y, Zr, Nb, and Pb were made with a Rigaku model 3062 spectrometer, following the methods of Bence and Albee (1968) and Norrish and Chappell (1977). Four NIST standard reference materials were run as unknowns to monitor analytical accuracy. Precision of analyses (1σ wt %), based on counting statistics for levels analysed in this study for major elements is: $SiO_2 \pm 0.3$; $TiO_2 \pm 0.01$; $Al_2O_3 \pm 0.17$; $Fe_2O_3 \pm 0.1$; MnO $\pm$ 0.01; MgO $\pm$ 0.3; CaO $\pm$ 0.08; $Na_2O \pm 0.03$; $K_2O \pm 0.03$. For trace elements, precision of analysis (1σ in ppm) is: Nb $\pm$ 1; Th, Y $\pm$ 2; Sr $\pm$ 3; Rb, Zr $\pm$ 4.

Samples analysed by neutron activation analysis were irradiated at University of Missouri Research Reactor, and counted at New Mexico Institute of Mining and Technology, using high purity coaxial germanium detectors. SRM 1633-A was used as a standard. Sample preparation and data reduction follow Jacobs et al. (1977) and Korotev and Lindstrom (1985). Standard reference materials BCR-1 and G-2 were analysed to monitor analytical accuracy and procedure. Analytical precision for elements reported in this study, to 1σ as determined by counting statistics, is (all in ppm, except where noted otherwise): Na $\pm$ 0.02 wt %; Ba $\pm$ 20; La $\pm$ 1; Sm $\pm$ 0.09; Yb $\pm$ 0.06; Lu $\pm$ 0.01; U $\pm$ 0.02; Sc $\pm$ 0.13; Fe $\pm$ 0.05; Co $\pm$ 0.16; Zn $\pm$ 4; Rb $\pm$ 3; Cs $\pm$ 0.06; Nd $\pm$ 2; Eu $\pm$ 0.02; Hf $\pm$ 0.1; Ta $\pm$ 0.03, Th $\pm$ 0.1.

Electron microprobe analyses

Electron microprobe analyses of ISV rock samples were made with a Cameca SX-50 microprobe at the University of Tennessee, using ZAF correction procedures. An excitation potential of 10 kV, and a beam current of 20 nA were used with natural and synthetic standards, as well as with the unknowns. The beam size was adjusted to accomodate the sample type, generally a 20 μm diameter beam was used for glassy areas and a 5–10 μm beam for crystals. During calibration, an intermediate (10 μm) beam size was used. Reference materials KN-18 and KE-12 were used to monitor analytical accuracy. Precision of analysis, based on counting statistics (1σ wt %), at the levels of analysis in this study is: $SiO_2 \pm 0.5$; $TiO_2 \pm 0.1$; $Al_2O_3 \pm 0.2$; FeO $\pm$ 0.3; CaO $\pm$ 0.5; MgO $\pm$ 0.3; $Na_2O \pm 0.2$; $K_2O \pm 0.2$; and MnO $\pm$ 0.1.

Results

Thermal history of the melt

The thermal evolution of the melt recorded by a representative type-C thermocouple during heating, melting and cooling is shown in Fig. 2. The temperature of the soil, initially at ambient temperature ($\sim$16° C), increased rapidly to 100° C as the front of boiling water ahead of the melt approached the thermocouple position 15 h after heating started. A thermal hiatus occurred at 100° C while pore water in the soil boiled. The variations in temperature from 100° C during the 30–50 h time period were probably a result of water circulation around the boiling zone. Once most water was converted to steam, heating to melt temperature was rapid (t = $\sim$60 h).

The maximum melt temperature recorded was approximately 1500° C. The cooling event apparent at $\sim$80–90 h (Fig. 2) was the result of an extended power failure during which the temperature of the melt dropped below 1200° C. Heating to 1500° C was rapid once the power was restored. Upon termination of power at the end of the test (127.5 h after initial melting began), the temperature of the melt dropped rapidly, at roughly 0.005° C/s to $\sim$1200° C. During this cooling interval, several thermal perturbations (rapid temperature drops followed by recovery to previous levels), were recorded

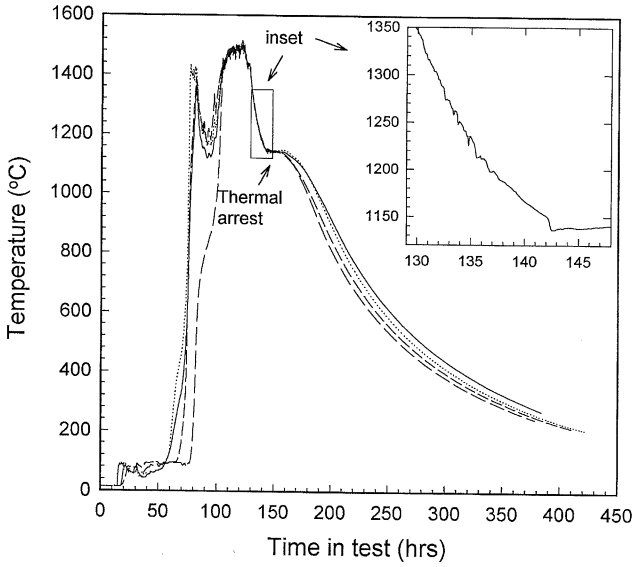

Fig. 2 Thermal evolution within the ISV melt as recored by 4 thermocouples at approximately the same depth within the melt, but each located 90° apart. Note thermal similarity during final melt and initial cooldown times. *Inset* shows detail of thermal evolution between temperatures of 1120 and 1350°C

within the melt between 1350 and 1200° C (Fig. 2, inset). These perturbations were recorded by all 4 type-C thermocouples and represent temperature variations of up to 10° C. Each perturbation was recorded during several sequential measurements of temperatures, thus it is unlikely that they represent either analytical uncertainty or electronic spikes of the thermocouples. Furthermore, although the thermal perturbations cannot be exactly correlated in time between the 4 type-C thermocouples, all recorded perturbations are the same temperature interval. Between ~1200 and 1150° C, cooling proceeded at a slower rate (~0.0027° C/min) than observed earlier. At 1140° C, cooling ceased for between 16 and 24 h (times are different for different type-C thermocouples). Temperature variations recorded by 2 of the 4 thermocouples indicate a rapid temperature decrease and then increase just before the thermal arrest (Fig. 2, inset). The temperature during thermal arrest increases slightly over the period of thermal arrest for 2 of the 4 thermocouples. Following the thermal arrest, cooling progressed at ever-decreasing rates.

Distribution and appearance of crystals

The geometry of the ISV rock body was determined by core drilling (Fig. 1). The shape is roughly hemispheric, but is slightly elongate in one direction, probably a result of the geometry of a rectangular-shaped trench that was placed within the melt area. The melt elongation appears to be in the same orientation as trench elongation, suggesting that the trench influenced melting patterns. The rock body is ~3 m in diameter, up to ~1.5 m thick, and attained a final depth of ~2.7 m below the ground surface. Mass balance calculations based on initial limestone and soil compositions and final rock compositions (Table 1) suggest that approximately 80% soil and 20% limestone were incorporated into the final melt.

The ISV rock is dominated by pyroxene, plagioclase and potassic feldspar crystals, but contains a small amount of dark green glass along the outer margins of some parts of the rock body. In the interior, acicular pyroxene crystals up to 10 mm long and 1 mm wide are visible in hand sample. These crystals are arranged in radiating masses throughout much of the body, although they are best developed in the center (Fig. 3a). Voids are present between masses of crystals, presumably resulting from volume reduction during crystallization. The amount of void space correlates roughly with the size of crystals and degree of crystallinity and is highest in the central part of the body. An area of largest crystals and highest pore space was delineated within the central part of the rock body (Fig. 1). This zone is not centrally located, but is slightly offset towards the upper surface of the rock body. A basal zone of finer crystals appears to be uniformly ~50 cm thick. The uppermost surface of the crystallized melt is characterized by small (<5 mm) spherulitic masses of crystals in a glassy matrix.

Examination of polished sections in reflected light reveals the presence of four identifiable phases; pyroxene, plagioclase feldspar, potassic feldspar and glass. A few small (~1 μm), highly reflective blebs, possibly reduced Fe, are present in some parts of the most crystalline samples.

The size, distribution, and abundance of crystals changes systematically with position of the sample within the rock body, but some features were common to all areas (Fig. 3a–e). A bimodal size distribution of crystals is always present; large (up to 1.5 cm in length) pyroxene crystals dominate the assemblage, with interstices filled with a "groundmass" (GM) assemblage consisting of plagioclase, pyroxene and glass ± potassic feldspar. Potassic feldspar is present only in the most crystalline, central part of the rock body. Pyroxene crystals in the core of the body are present as large, acicular crystals arranged in radiating masses (Fig. 3a,c). Pyroxenes also dominate samples from nearer the edge, but the crystal size is much smaller, and crystals are more closely spaced than in the central part of the rock body (Fig. 3e). The pyroxene crystals in the edge zones still appear to have grown in skeletal clusters, but the distinct radiating habit observed in the central zone samples is not present. Samples from intermediate zones contain intermediate-sized (up to 8 mm long) and spaced acicular pyroxene crystals which also occur as discrete radiating, sheaf-like clusters (Fig. 3b,d). Within the GM assemblage, plagioclase appears to make up around 60% of the total assemblage.

Table 1 Major and trace element analyses of sample from the rock body, and pre-melt soil and limestone (*n* number of analyses)

	Rock n = 23		Soil n = 9		Limestone n = 2	
	Mean	SD	Mean	SD	Mean	SD
X-ray fluorescence wt%						
SiO_2	52.10	0.17	62.44	2.12	14.02	2.15
TiO_2	0.75	0.01	0.88	0.03	0.06	0.02
Al_2O_3	15.70	0.16	19.02	0.82	2.70	0.24
FeO	4.85	0.13	6.35	0.24	0.94	0.13
MnO	0.12	0.00	0.14	0.03	0.07	0.01
MgO	5.94	0.24	2.63	0.30	30.40	0.16
CaO	16.96	0.20	4.28	2.61	50.30	1.66
Na_2O	0.20	0.06	0.20	0.09	0.00	0.00
K_2O	3.26	0.05	3.93	0.16	1.51	0.03
P_2O_5	0.11	0.01	0.13	0.01	0.01	0.00
LOI	0.18	0.47	9.57	1.66	41.78	0.00
Total	99.22	0.86	98.53	0.48	95.01	1.99
X-ray fluorescence analyses (all in ppm)						
Th	11	2	12	1	0	0
Rb	109	2	123	5	8	1
Sr	153	2	72	16	94	8
Y	37	1	48	16	2	1
Zr	249	3	249	9	18	0
Nb	16	0	15	0	5	0
Neutron activation analyses (in ppm unless noted)						
Na(wt%)	0.22	0.05	0.29	0.04	0.03	0.01
Sc	13.92	0.37	14.79	0.96	0.90	0.00
Fe	4.75	0.04	5.55	0.32	0.45	0.02
Co	13.97	0.10	21.29	3.28	3.59	2.29
Zn	172	5	93	4	1490	937
Rb	109	3	126	8	9	1
Cs	3.72	0.10	4.14	0.24	0.21	0.02
Ba	425	21	411	19	39	7
La	137.8	2.0	49.1	6.0	3.5	0.0
Nd	102.8	2.8	48.3	12.8	2.0	0.0
Sm	8.22	0.08	10.45	3.2	0.48	0.05
Eu	1.74	0.02	2.22	0.7	0.10	0.07
Yb	3.33	0.10	4.08	0.98	0.16	0.02
Lu	0.496	0.015	0.587	0.122	0.024	0.002
Hf	7.08	0.08	7.41	0.38	0.33	0.02
Ta	0.782	0.020	0.844	0.061	0.086	0.025
Th	10.19	0.18	10.94	0.66	0.84	0.15
U	2.6	0.2	2.5	0.2	0.850	0.071

The size of the GM crystals varies with position of the sample within the rock body, with the largest crystals present in the core of the rock body. Plagioclase crystals from the center of the body are around 0.03 mm in size, and pyroxene around 0.02 mm. In some samples from nearest the body's edge, this GM assemblage is virtually absent, and the interstices between the large pyroxene crystals contain only glass.

The shape of crystals also varies systematically as a function of sample location. Within the central part of the body, the large pyroxene crystals are acicular and flat-sided, with length to width ratios of up to 25:1 (Fig. 3a, c). Pyroxene crystals nearer the body's edge are generally smooth-sided, but the last-deposited crystal margin appears to have grown skeletally, and forms finger-like protrusions off the otherwise-flat sides. With increasing proximity to the edge of the melt, pyroxene growth becomes less acicular, and more skeletal and dendritic (Fig. 3d, e). Although the grain size of the GM pyroxene and plagioclase crystals decreases with proximity to the edge of the body, their shape does not appear to change.

Chemical composition of crystalline phases

The pyroxene crystals range in composition from diopside, a magnesian pyroxene, to hedenbergite, a Fe-rich pyroxene (Fig. 4, Table 2). The recalculations of pyroxene compositions for the ternary diagram were made including Ti, Mn, and non-tetrahedral Al in the Fe-pyroxene endmember (Lindsley 1983). The cores of the large pyroxene crystals are composed of homogeneous diopside, but a thin rim of last-grown crystal is Fe-rich hedenbergite (Fig. 5; trend B of Fig. 6). The transition from the diopsidic core to hedenbergitic rim is sharp.

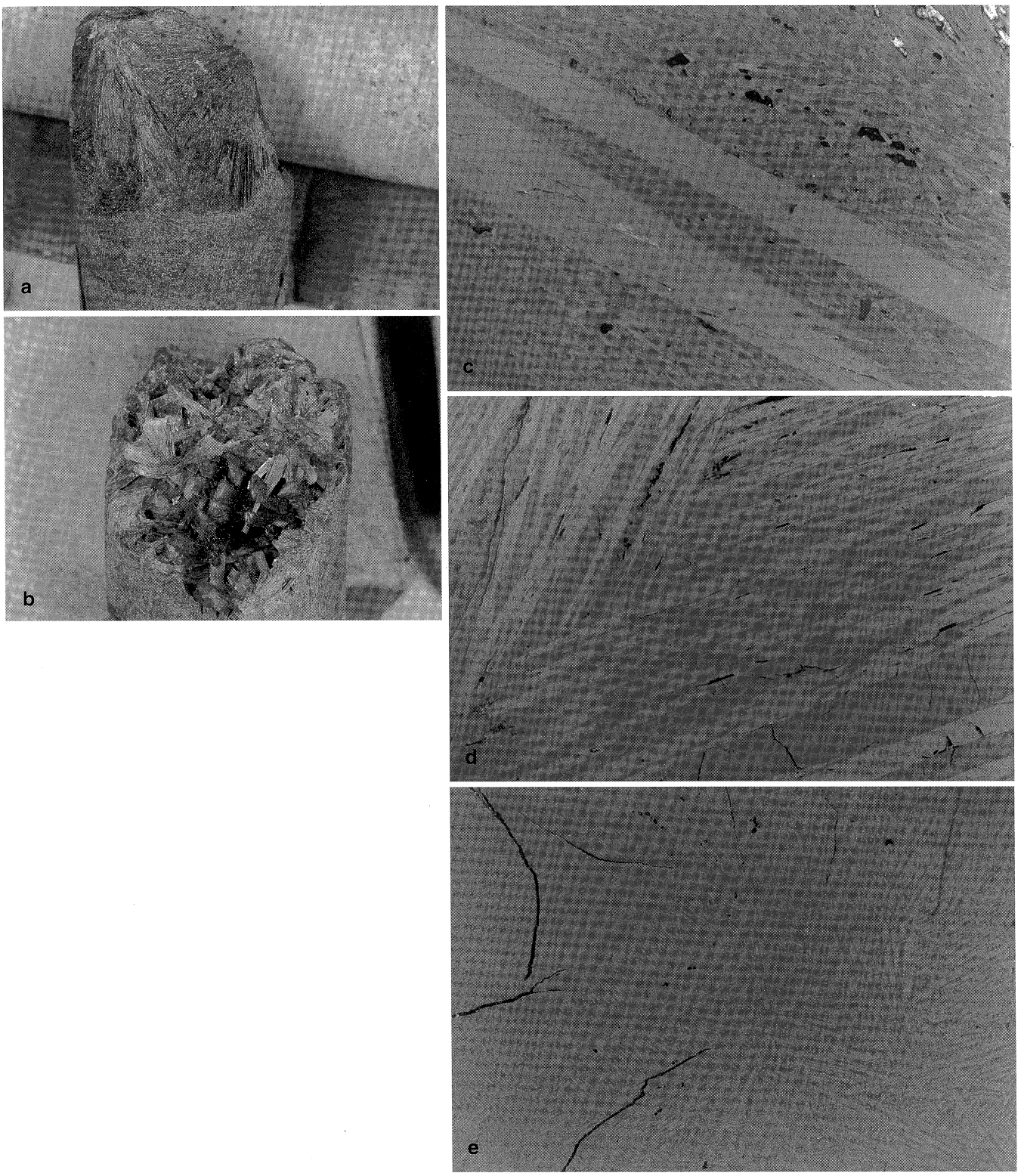

Fig. 3a-e Photographs of crystalline ISV samples. **a** Core sample from the central part of the melt showing large acicular pyroxene crystals. Core is 1″ diameter. **b** Core sample from an intermediate part of the melt, showing sheaf-like masses of pyroxene crystals. **c-e** Reflected-light photomicrographs of samples of ISV rock taken a various distances from the margin. Field of view of all photos is 1mm. Highest reflectivity phase is pyroxene, intermediate reflectivity is plagioclase, and lowest reflectivity areas are mixtures of glass plus potassic feldspar. All phases are not visible in samples nearest the rock margin. **c** Core of melt. **d** 1/2 distance between core and edge. **e** Near edge of melt

The groundmass pyroxene crystals are also composed of diopsidic cores and hedenbergitic rims, but detailed zonation profiles are difficult to determine because of their small size. BSE images suggest that the diopside to hedenbergite transition is also sharp in the groundmass pyroxene. The composition of the diopsidic pyroxene varies subtly with distance from the center of the rock body (Fig. 6). The cores of pyroxene crystals from the central part of the body are slightly more Mg-rich, but Fe- and Al-poor (trend A on Fig. 6), than those from the outer part of the body. Ca content is approximately the same in all pyroxene.

Groundmass plagioclase is anorthitic in composition ($An_{86}Ab_4Or_{10}$), and appears to be homogeneous throughout (Fig. 7, Table 2). Potassic feldspar, where present, is orthoclase ($An_{10}Ab_3Or_{87}$) (Fig. 7, Table 2). Several points in Fig. 7 which appear to fall in the two-feldspar field are likely to represent a composite analysis of two adjacent feldspar phases.

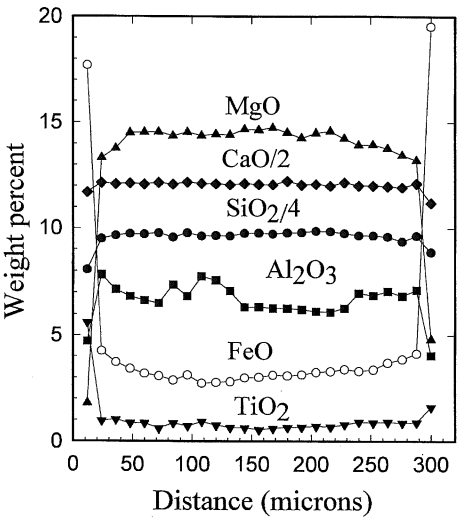

Fig. 5 Electron microprobe step-scan analyses across a single pyroxene lath from the central part of the ISV body

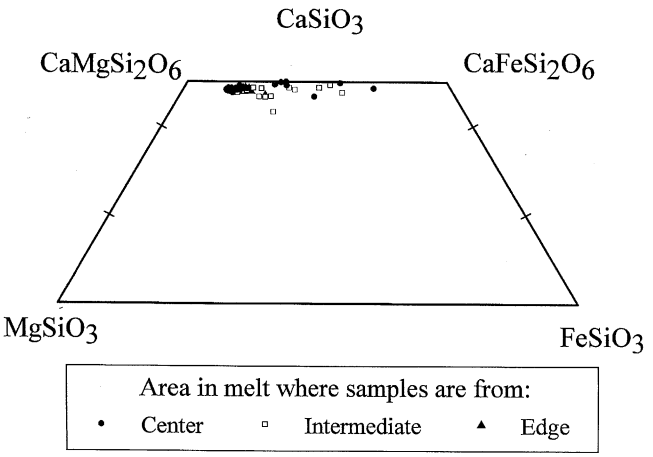

Fig. 4 Pyroxene compositions as analyzed by electron microprobe displayed on standard pyroxene quadrilateral diagram. The recalculations of pyroxene compositions for the ternary diagram were made including Ti, Mn, and non-tetrahedral Al in the Fe-pyroxene endmember (Lindsley 1983)

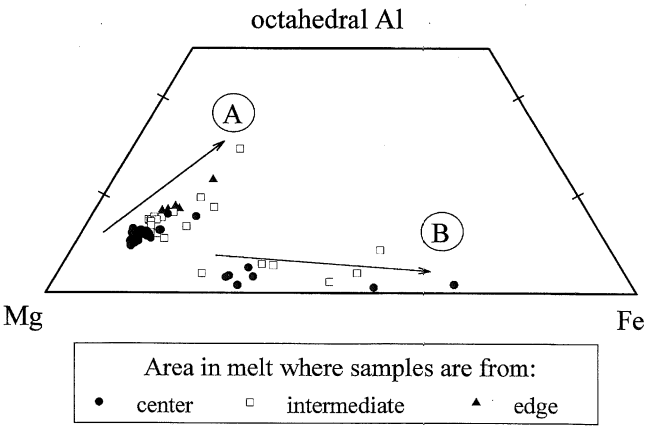

Fig. 6 Pyroxene compositions as analyzed by electron microprobe expressed as a ternary of octachedral Al, Fe, and Mg. Two compositional trends are indicated, one labelled *A* and the other labelled *B*. The *A* trend represents a compositional trend towards lower Mg and higher Al, and the *B* trend represents low Mg and high Fe that are observed in crystal rims

Table 2 Representative electron microprobe analyses of phenocryst compositions

Phase	SiO_2	TiO_2	Al_2O_3	MgO	CaO	MnO	FeO	Na_2O	K_2O	Total	An	Ab	Or
Pyx 1[a]													
Core	48.7	0.9	6.8	14.5	24.2	0.1	3.4	0	0	98.6			
Rim	47.0	1.9	4.4	6.9	23.2	0.3	15.5	0	0	99.2			
Pyx 2[b]	48.4	0.8	8.2	13.7	24.6	0.1	3.4	0	0	99.2			
Pyx 3[c]	47.2	1.1	9.9	12.6	24.3	0.1	4.3	0	0	99.6			
GM Pyx[d]	48.8	1.4	4.7	11.4	24.0	0.2	8.8	0	0	99.3			
GM Plag[e]	47.3	0	31.8	0.5	17.2	0	0.8	0.5	1.6	99.7	86	4	10
GM Orth[f]	62.1	0.2	20.2	0	2.0	0	0.3	0.3	14.7	99.8	10	3	87

[a] large pyroxene from rock center
[b] large pyroxene from intermediate zone between rock center and edge
[c] pyroxene from near rock edge
[d] groundmass pyroxene
[e] groundmass plagioclase
[f] groundmass orthoclase

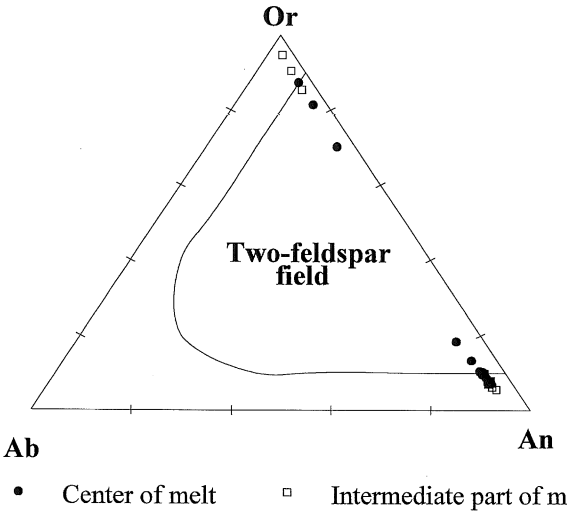

Fig. 7 Feldspar compositions as analyzed by electron microprobe expressed as orthoclase, albite, and anorthite endmembers

Discussion

Melting processes and convection

The homogeneity of the ISV rock suggests that convective mixing was effective during the melting process. The strongest evidence for complete mixing during the melting process is the homogeneous distribution of rare earth element tracers, which were placed different depths in the projected melt volume, and were therefore incorporated into the melt at different times during the melting process. Although high temperature adjacent to the electrodes is the main driving force, convection affected the entire molten mass, as evidenced by the compositional similarity of samples in thin lateral limbs of the rock body that one might think could be convectively isolated from the melt's central area. Furthermore, rock samples from within a few centimeters of the margin of the rock body are compositionally identical to the core of the body, suggesting that a wide, compositionally isolated partial melt zone, such as might be present in a larger melt, was absent. The observed partial melt zone from core samples is ~1–2 cm thick.

The rapid and complete convection within the small melt body is likely to result from the relatively low melt viscosity. The viscosity at a melt temperature of 1400°C is calculated to be 97 poise (using methods of Shaw 1972), which is low compared to many natural magmas. For comparison, the viscosity of a dry Hawaiian basalt at a temperature of 1200°C is ~280 poises (Ryan and Blevins 1987), so the ISV melt is probably less viscous than most natural magmas, and would hence be expected to convect vigorously.

During cooling of the ISV melt, distinct thermal oscillations with a 10–20 min period, and temperature variations of 10–20°C, are observed at temperatures between 1325 and 1210°C. Thermocouples near the melt margin measured less distinct oscillations. These oscillations are interpreted to be a result of slowing convection within the melt, where sequentially hotter and cooler melt in different parts of the convection cell move past the thermocouples (Jacobs et al. 1993). The thermal oscillations dampen near the liquidus temperature, and cease completely slightly below the liquidus, which is 1202° based on the MELTS model (Ghiorso 1987; Ghiorso and Carmichael 1987). Based on the observed thermal behavior, estimated convection rates were 0.004 m/s during cooling from 1400–1325°C, 0.0016 m/s from 1325–1210°C, and 0.0004 m/s near the liquidus.

Crystallization

The crystallization process within the ISV melt produced features that have been observed experimentally, as well as within natural systems. Most striking was the feedback between crystallization and the thermal evolution of the melt. The marked hiatus in cooling that occurs between 140 and 160 h (Fig. 2, termed "thermal arrest") is interpreted to be a result of exothermic heat of crystallization, and highlights the significant effect that crystallization could have on the thermal evolution of a natural magmatic system. The thermal arrest period may be exaggerated because of the rapid cooling rates and high initial temperature by analogy to work discussed by Lange et al. (1991).

Crystal nucleation and growth

As discussed earlier, it is probable that the ISV melt was physically and chemically homogeneous at the time that cooling was initiated (127.5 h). Therefore, all variations of crystal shape and composition must be solely a function of cooling rate and its effect on undercooling during crystal growth within different parts of the melt. Crystal shape within the ISV rock varies systematically as a function of distance from the melt-soil boundary. The variations of crystal shape are similar to those described by Lofgren (1980), with tabular forms dominant in the central area of the body, changing progressively to dendritic and spherulitic forms nearer the edge (Fig. 3c–e). These variations can be attributed either to variations in cooling rates or to degree of undercooling at the time that crystallization was initiated (Lofgren 1980). Some crystals, particularly in areas of the melt mid-way between the core and the edge, are characterized by initial growth in a faceted habit followed by skeletal growth of the outer part of the crystal. This change may be due to rapid cooling that occurred following thermal arrest (Fig. 2).

The ISV rock body is characterized by a porphyritic texture, similar to that observed in some extrusive volcanic rocks, with a set of large pyroxene crystals and a groundmass of fine-grained pyroxene, plagioclase, orthoclase and glass. In volcanic rocks, this texture is clearly a result of the presence of pre-existing phenocrysts at the time of eruption, and subsequent growth of GM crystals (e.g., Cashman 1992). However, in the case of the ISV melt, no initial population of phenocrysts was present to explain this texture. Simple homogeneous nucleation and growth of a single crystal population seem unlikely to explain the observed crystal size characteristics. However, in experimental studies on lunar basalts, porphyritic textures were produced from an initially homogeneous melt (Lofgren 1980). As the melt cools, the first phase on the liquidus, in this case diopside, nucleates and begins to grow. The presence of a single phase initially on the liquidus is important in producing this texture (Hort and Spohn 1991). As diopside growth continues, the residual melt composition changes, and the melt further cools, until the liquidus of a second phase, in this case anorthite, is reached. At this point, large-scale saturation and growth of anorthite would occur, causing another change in the residual melt composition, causing renewed supersaturation of pyroxene, allowing a second stage of pyroxene nucleation and growth. The final texture would appear similar to that observed in the ISV melt: a dominant first generation of pyroxene, and a groundmass of plagioclase and pyroxene, slightly dominated by plagioclase. However, if pyroxene and plagioclase had both begun crystallizing simultaneously, the porphyritic texture would not have been produced. These observations also suggest that polymodal crystal size distributions within a plutonic body can be a result of a slowly-cooled chemically and physically homogeneous magma body, and that it is not necessary to call on dramatic physical or chemical changes, such as pressure and/or P_{H_2O} changes during crystal growth to produce this type of crystal size distribution.

Timing of crystal growth

Evidence from thermal behavior of the melt

The cooling histories recorded by thermocouples in the central part of the IVS melt (Fig. 2) lend some insight into the timing of crystallization. Due to the rapid convection during active melting (convection rate $\sim$0.1 m/s), the melt is likely to have been thermally homogeneous. Once cooling began, the initial cooling rate was approximately -0.005°C/s. This average rate was relatively constant until around 1200°C, when the cooling rate slowed to -0.0027°C/s. The change in cooling rate did not occur gradually, but can be seen as a slight bend in the measured cooling curve shown in Fig. 2. At the same time as the cooling rate changed, convection in the melt, as recognized by thermal oscillations became strongly dampened, and may have even ceased (Fig. 2). The change in cooling rate and dampening of convection are interpreted to be a result of the first growth of pyroxene crystals, and this temperature is nearly coincident with the liquidus temperature of 1202°C for the ISV-composition melt derived from the MELTS model (Table 3). The lack of convection once crystallization begins is suggested by the thermal evidence for dampening of convective movement, but indirect evidence can also be gained by observations of crystal shape. The large first generation (FG) pyroxene crystals in the central and intermediate portions of the ISV rock are very delicate acicular crystals arranged in sheaf-like or radiating masses (Fig. 3a, b). These masses show no evidence of being disrupted once crystal growth began, and no evidence is found of broken crystals, whereas if vigorous convection was still active at the time of crystal growth, evidence of these two phenomena would certainly be seen. This lack of convection near the liquidus is consistent with experimental evidence discussed by Brandeis and Marsh (1989).

During the period of cooling between about 1210°C and 1140°C, the cooling rate of the melt appears to be only slightly slowed by latent heat contribution due to crystallization, as evidenced by the only slight change in cooling rate during this interval. This decreased cooling rate, while not as dramatic as the long thermal arrest, may be due to latent heat input by initial pyroxene growth and suggests that only a small amount of crystallization was taking place during this time. At 1140°C, the crystallization rate apparently becomes much higher, as evidenced by the sudden flattening of the cooling curve, due to a higher rate of latent heat evolution. This period is likely to represent pseudocotectic crystallization of the two major phases, plagioclase and pyroxene, and although MELTS modelling suggests that plagioclase may form at higher temperatures, widespread plagioclase growth probably does not take place until this temperature. The possibly lower thermal arrest temperature recorded by thermocouples nearer the edge of the melt could be due to suppression of plagioclase nucleation in the faster cooling regime (e.g., Grove and Bence 1977; Lofgren 1983). The overall thermal history supports the multistage crystal growth hypothesis suggested earlier, with a second generation of pyroxene crystals also growing at this time, as suggested by textural evidence.

Evidence from MELTS and thermal modelling

The two types of modelling, the MELTS model (Table 3; Ghiorso 1987; Ghiorso and Carmichael 1987), and thermal modelling (Alexiades and Jacobs 1994), reinforce the conclusions about timing of crystallization made on the basis of thermal history of the melt and textural evidence for sequence of crystallization.

The results for the MELTS modelling are summarized in Table 3, and in the following sentences. The pyroxene liquidus temperature calculated by MELTS is 1202°C for iron-wüstite redox conditions. Diopsidic pyroxene ($Tsch_8Di_{80}Hd_{12}$), the primary liquidus phase, is joined by anorthitic plagioclase ($An_{95}Ab_{40}Or_1$) in the interval 1202–1197°C, and both phases coexist throughout the remainder of the calculated crystallization history.

Although the thermal model does not allow determination of crystal compositions to be made, it does allow some estimates of timing of crystal growth. In this model the melt composition is modelled as a diopside-anorthite binary (Alexiades and Jacobs 1994). A cooling curve similar to those observed for the ISV melt was produced (Fig. 8), as well as a cooling curve for simple conductive cooling of the melt with no latent heat input. As can be seen by comparing the actual cooling curve with a cooling curve calculated for simple conductive cooling, with no latent heat contribution (Fig. 8), the two curves begin to diverge slightly at the liquidus temperature of ~1210°C, close to the MELTS-calculated liquidus temperature of 1202°C, suggesting that some latent heat is being input due to initial pyroxene growth. The small amount of divergence observed between actual and calculated cooling curves from 1210°C to 1140°C suggests that the degree of crystallization during the interval between the pyroxene liquidus and the large-scale crystallization that produced the thermal arrest is small. Once the thermal arrest temperature of 1140°C is reached, the two cooling curves diverge sharply (Fig. 8), indicating a larger input of latent heat input, and thus a much larger amount of crystallization. Although it is not possible to estimate the relative percentages of crystallization as a function of temperature using this model, the relative importance of latent heat input due to crystallization before the thermal arrest is insignificant compared to that once the thermal arrest has begun. The MELTS model suggests that the system is 56% crystalline at a temperature of 1142°C, reinforcing the conclusions that a large amount of crystallization takes place during the thermal arrest. Although based on thermal behavior of the melt alone, it is not possible to predict when crystallization ends, MELTS suggests that crystallization is nearly complete by ~1000°C. This temperature is used as the solidus temperature for the following calculations of crystal growth rates.

Table 3 Summary of observations from the ISV experiment and the results of MELTS modelling

ISV Product	MELTS modelling
Pyroxene ($Tsch_{19}Di_{74}Hol_7$)	1202°C pyroxene ($Tsch_8$ $Di_{80}Hol_{12}$)
Plagioclase ($An_{86}Ab_4Or_9$)	1197°C plagioclase ($An_{95}Ab_4Or_1$)
Thermal arrest 1137–1147° C	1142°C pyroxene + plag (56wt%) 1142–1017°C leucite
K-feldspar ($An_{10}Ab_3Or_{86}$)	1022° C K-feldspar ($An_4Ab_5Or_{91}$)
Glass (65-71 wt% SiO_2)	Liquid (62wt% SiO_2)
Analysed mode	MELTS mode at 1002°C
Pyroxene 50%	Pyroxene 48%
Plagioclase 28%	Plagioclase 27%
K-feldspar 10%	K-feldspar 14%
Glass 12%	Liq 11%

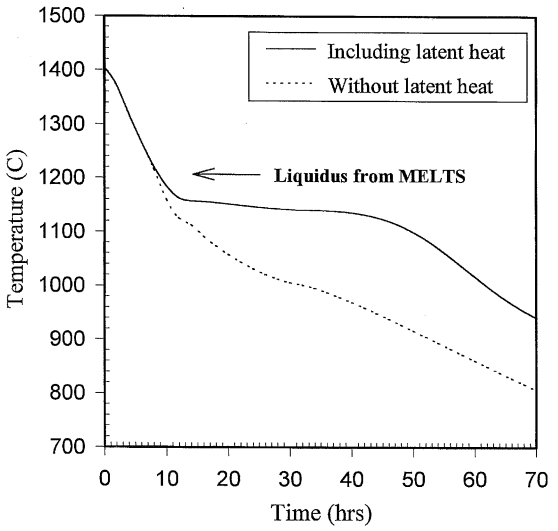

Fig. 8 Results of thermal modelling, showing a model cooling curve for the melt including the latent heat of crystallization, and a second cooling curve for simple conductive cooling without latent heat of crystallization input. Liquidus temperature calculated from MELTS model is indicated.

Crystal growth rates

Estimates of the growth rates for pyroxene and plagioclase crystals from the center of the ISV melt can be made based on timing of cooling anomalies interpreted to be the result of crystallization, and size of crystals. The largest pyroxene crystals in any sample are assumed to begin growth at 1202°C (t = 136.5 h), based on the change in melt cooling rate and MELTS thermodynamic calculations, and the plagioclase and groundmass pyroxene crystals are assumed to begin growth at the beginning of the thermal arrest period, at approximately 1140°C (t = 143 h). Significant growth of both phases is assumed to cease slightly after the end of the thermal arrest period, at ~1000°C (t = 190 h). The largest single pyroxene crystals observed in the core of the rock body are ~9 mm in length, and ~1 mm in width. The thermal history of samples from the core of the melt is best known, because of the presence of 4 type-C thermocouples and this is where growth rates can be determined with the greatest degree of accuracy.

The growth rates estimated for the ISV crystals (Table 4), between 10^{-7} and 10^{-8} cm/s, are slower than experimentally-determined maximum growth rates for

Table 4 Crystallization rates from the center of the ISV body

Sample position	Crystal type	Size[a] (cm)	Start (h)	End (h)	Growth time (h)	Growth rate (cm/s)
Determined based on thermocouple record						
Center	FG pyrox[b]	0.1	136.5	190	53.5	1×10^{-7}
Center	GM pyrox[c]	0.002	143	190	47	1×10^{-8}
Center	GM plag[d]	0.003	143	190	47	2×10^{-8}

[a] The crystal sized reported are crystal widths, not lengths, for tabular crystals
[b] Large "first generation" pyroxene crystals
[c] Groundmass pyroxene
[d] Groundmass plagioclase

crystals in some similar systems (e.g., Dowty 1980), and are faster than, or similar to, rates determined for natural systems (Cashman and Marsh 1988), reflecting cooling rates and degree of undercooling for the central part of the ISV melt intermediate between small experimental and large natural systems. The growth rate for the ISV crystals falls on a curve of growth rate vs cooling rate defined by a set of natural systems (Cashman 1993). The size of the ISV body provides a good analog for a small magma body, such as a dike, or the edge zone of a larger magma body. The change in the character of the rock at about 50 cm from the rock body's edge (Fig. 2), from friable and less crystalline to harder and more crystalline agrees quantitatively with that predicted by Hort and Spohn (1991) in a dike setting. They ascribe the crystallinity difference to equilibrium versus disequilibrium crystallization, and in the ISV case, a higher proportion of uncrystallized residual glass also appears to be present in the outer 50 cm.

The fastest observed growth rates are for the largest pyroxene crystals that grew in the central part of the body. The size used for calculation is the maximum observed size, and many of the large central pyroxenes are smaller, but still yield growth rates higher than the groundmass phases. These pyroxene crystals in the center of the melt would have begun to grow during a time of rapid cooling, but low degree of undercooling, during which the nucleation rate was apparently low and the growth rate high. The smaller, but more numerous groundmass pyroxene crystals in the center of the melt, which nucleated and grew during the thermal arrest at a high degree of undercooling relative the their liquidus temperature would have a high nucleation rate, but lower growth rate (1×10^{-8} cm/sec), and hence many, very small crystals. This behavior is consistent with known nucleation and crystal growth behavior (e.g., Winkler 1947).

According to the MELTS model, plagioclase should have begun to nucleate very shortly after the FG pyroxene crystals. However, textural evidence suggests that this did not happen, but that plagioclase nucleation was suppressed until an undercooling of 55° was reached (thermal arrest temperature), at which time a large pulse of nucleation occurred. Plagioclase nucleation has been reported to occur at high degrees of undercooling in natural systems as well, due to a reluctance to nucleate (e.g., Lofgren 1980). The apparently faster growth rate of GM plagioclase relative to GM pyroxene (Table 4), although similar growth rates might be expected, suggests that the GM pyroxene may have begun to nucleate and grow later that the plagioclase. This growth sequence would be consistent with a renewed supersaturation of the melt with respect to pyroxene following the major episode of plagioclase growth. Petrographic evidence supports this conclusion, because the groundmass pyroxene crystals appear to grow interstially between the groundmass plagioclase.

Crystal chemistry

Comparison with MELTS modelling

Equilibrium phase relations calculated with the thermodynamic model MELTS (Ghiorso 1987; Ghiorso and Carmichael 1987) provide estimates of the initial crystallization temperatures in the ISV system, but also estimates the mineral composition and modal proportions are made with MELTS, which can be compared to measured compositions. Only these two phases crystallize during the first 60°C of cooling to 1142°C, producing solidification of 56 wt% of the system, which is consistent with widespread crystallization of the large artificial melt inferred from the observed thermal arrest over the range 1147–1137°C. The model also predicts crystallization of leucite at 1142°C and subsequent resorption at 1017°C, and resultant precipitation of sanidine ($An_4Ab_5Or_{91}$) beginning at 1022° from liquids having silica contents of 62 wt%, which is in agreement with the observed presence of a potassic feldspar in silica-rich interstitial glass in the ISV melt (Dunbar et al. 1993). In summary, the phase assemblage and proportions predicted by MELTS at 1002°C (14% pyroxene + 27% plagioclase + 14% potassic feldspar + 11% glass) are in very good agreement with the observed mineralogy and phase proportions calculated from the observed bulk and mineral compositions from Dunbar et al. (1993) (50% pyroxene + 28% plagioclase + 10% potassic feldspar + 12% glass).

Effect of growth rates on crystal composition

The phenocryst phases in the ISV melt are surprisingly homogeneous, particularly considering the rapid rates of crystallization. Although there are some variations in pyroxene composition, as will be discussed later, there does not appear to have been any *progressive* buildup or depletion of compatible or incompatible components at the crystal-melt interface during growth

of individual crystals, as has been suggested to occur during rapid crystal growth (Burton et al. 1953; Albarede and Bottinga 1972). In all cases where crystals are large enough to analyze, the compositions of plagioclase and K-feldspar appear to be independent of location within the melt, and therefore of growth rate.

Despite the overall homogeneity of individual crystals, some systematic variations in pyroxene compositions are observed. The first type of variation observed is the presence of Fe-rich rims on pyroxenes, mainly from the interior portions of the melt (Fig. 5). These rims are present on both FG and GM pyroxene indicating that deposition occurred during latest-stage crystal growth. The Fe-rich rims are also characterized by high Ti and slightly low Al with respect to Mg-rich compositions (Fig. 5). Ti is incompatible in all crystalline phases, so would be enriched in the evolved melt. The Al composition of the melt remains the same throughout, so the lower Al content of the Fe-rich pyroxenes is not a result of increasing Al in the melt, but may be instead related to charge balance associated with Ti substitution. Coupled substitution of $Ti^{VI}2Al^{IV}$ for $R^{VI}2Si^{IV}$ has been noted in other cases, particularly in lunar rocks (Bence et al. 1970). The rims may be a result of Mg depletion in the melt due to large-scale diopside growth. However, the sharp nature of the transition, rather than gradual transition to more hedenbergitic composition suggest that other factors may be involved in the rapid compositional change. Because the temperature remained constant for a long period of time during the thermal arrest, a single composition of pyroxene would be expected to crystallize as long as the Mg content of the melt remained relatively constant. Although the pyroxene crystals preferentially incorporate Mg, the Mg content of the residual melt may have remained relatively constant initially due to plagioclase crystallization. However, when the groundmass pyroxene began to crystallize, Mg in the melt would become strongly depleted. Modal calculations and analyses of residual glass (Dunbar et al. 1993) indicate that this is the case. As the Mg content of the melt became depleted, but temperature of the melt remained constant, pyroxene growth may have slowed, or even ceased. However, without the input of latent heat of crystallization, melt temperature dropped, reaching a temperature at which an Fe-rich pyroxene composition was stable (Deer et al. 1994). At this point, the final rim of hedenbergite would have been deposited.

The second type of compositional variation noted in pyroxene is a decrease in the Mg content and increase in Al content as a function of distance of the sample from the edge of the melt (Fig. 6). The Al contents of pyroxenes which grew nearer the edge of the melt are proportionately higher than those which grew in the core, although all pyroxenes which grew in a given part of the melt are homogeneous. This type of chemical variation, explained as substitution of $Al^{VI}Al^{IV}$ for $Mg^{VI}Si^{IV}$, has been observed in lunar samples (Gamble and Taylor 1980), and has been experimentally shown to be related to crystal growth rate (Grove and Bence 1977). In situations where crystal growth is rapid, slow-diffusing compatible elements, such as Mg, are not able to diffuse to the crystal-melt interface fast enough to maintain equilibrium, and relatively incompatible elements, such as Al, substitute into the pyroxene structure (Grove and Bence 1977). The higher Al contents of crystals near the edge of the melt suggests that crystal growth rates were faster near the melt edge. These rates were not directly measurable, but faster growth rates are consistent with the more dendritic nature of crystals near edge of the melt (Lofgren 1980).

The observed patterns of systematic pyroxene compositional variation with distance from the center of the melt, but homogeneity within a given sample, plus the overall homogeneity of plagioclase crystals, suggests that the diffusion profiles of compatible and incompatible elements relative to the crystal-melt interface are established early in the growth of a single crystal, and do not change significantly during crystal growth. This observation can help explain the lack of compositional zonation in very large crystals in magmatic systems, such as large (up to 10 cm) anorthoclase feldspar crystals, which grow in a convecting lava lake at Mt. Erebus, Antarctica (Kyle 1977). The cores of these crystals are thought to grow rapidly in a single growth episode, possibly as a result of H_2O loss from the melt (Dunbar et al. 1994), but show no systematic progressive chemical zonation. By analogy to the large, chemically-homogeneous crystals observed in the ISV melt, although it is possible that a chemical gradient was present at the crystal/melt interface of the growing Mt. Erebus anorthoclase crystals, this gradient may be established very soon after the crystal growth began, and may remain constant throughout the time that the crystal grew.

Conclusions

In-situ melting of a soil and limestone mixture produced a chemically and thermally homogeneous magma body, large enough to allow occurrence of processes that would occur in a large magma chamber, but small enough for thermal monitoring during cooling and sample in detail after cooling, thereby providing an intermediate link between natural and experimental crystallizing systems. During cooling of the melt, extensive crystallization occurred, producing an assemblage composed dominantly of pyroxene and plagioclase, with subordinate potassic feldspar and residual glass. The proportions of phases and phase compositions agree well with those predicted by the MELTS thermodynamic model (Ghiorso 1987). The observed porphyritic texture is interpreted to be a result of

progressive saturation of different crystalline phases as the melt cooled, with an initial stage of pyroxene growth, followed by plagioclase growth at undercooled conditions, triggering a second episode of pyroxene growth. Crystal shape varies as a function of position within the rock body, and shapes characteristic of disequilibrium cooling are dominant near the edge. Crystal growth rates for the largest pyroxene crystals within the central portion of the melt are estimated to have been near 10^{-7} cm/s, and the growth rates for the groundmass phases are around 10^{-8} cm/s. The high growth rate, but low nucleation rate of FG pyroxenes from the center of the melt is consistent with the high cooling rate, but low degree of undercooling, whereas the slower-growing, but easily nucleated GM pyroxene crystals would have been formed at slower cooling rates but higher undercooling. Textural and thermal evidence suggests that once the large acicular pyroxene crystals began to grow, convection in the melt was virtually non-existent, although up until that point, the melt had been convecting vigorously.

During melt cooling, a marked cooling hiatus, termed "thermal arrest" is observed, where the temperature of the melt remained constant for approximately 24 h. This cooling pattern is interpreted to be the result of exothermic heat of crystallization, and suggests that the crystallization patterns within a magmatic system can have a strong effect on the cooling behavior.

Compositions of individual crystals in the ISV rock are remarkably uniform, although there is some evidence of chemical disequilibrium at the crystal-melt interface observed in pyroxene compositions, seen by comparing pyroxene compositions from the core and the rim of the melt. No chemical variability is observed within any plagioclase crystals, although the growth rates were vary fast, indicating that no progressive chemical disequilibrium at the crystal-melt interface developed as a function of time. Although individual pyroxene crystals are generally homogeneous (discounting Fe-rich rims formed at low temperature), pyroxene compositions are more magnesian in the core of the melt body, and more alumina-rich nearer the edges. This is consistent with observations of Grove and Bence (1977) that faster growth rates should favor more aluminous, less magnesian pyroxene compositions. Furthermore, the observed variations in pyroxene composition illustrate the wide compositional variations possible in crystals grown from a single melt composition, as a result of some variable controlling crystal growth, such as cooling rate or degree of undercooling. These observations also highlight the point that all crystal composition variation in natural systems is not necessarily a result of magmatic compositional variation.

Acknowledgements We would like to thank Mark Ghiorso for the MELTS thermodynamic modelling that was done as part of this study, and Vasili Alexiades and Alan Solomon for providing the thermal modelling. Thanks to Alan Patchen and Larry Taylor for assistance with the electron microprobe and Philip Kyle for assistance with XRF and NAA. Discussions with the above-mentioned people and other helped improve and focus the ideas presented here. Thanks to Katherine Cashman and two anonymous reviewers for insightful comments that helped to direct and focus our thinking. The research presented in this paper was supported by the Geosciences Research program of DOE's Office of Basic Energy Science. The ISV technology was developed and patented by Battelle Pacific Northwest Laboratory for the United States Department of Energy. The ISV test, sponsored by DOE's Office of Technology Development, was performed jointly with PNL. ORNL is managed by Martin Marietta Energy Systems, Inc., for DOE under contract DE-AC05-84OR21400.

References

Albarede F, Bottinga Y (1972) Kinetic disequilibrium in trace element paritioning between phenocrysts and host lava. Geochim Cosmochim Acta 36: 141–156

Alexiades V, Jacobs GK (1994) Solidification modelling of In Situ Vitrification melts. In: Ladde GS, Sambandham M (eds) Proceedings of Dynamic Systems and Applications Vol. 1 Dynamic Publishers, Atlanta, pp 11–16

Bence AE, Albee AL (1968) Empirical correction factors for the electron microanalysis of silicates and oxides. J Geol 76: 382–403

Bence AE, Papike JJ, Prewitt CT (1970) Apollo 12 clinopyroxenes: chemical trends. Earth Planet Sci Lett 8: 393–399

Brandeis G, Marsh BD (1989) The convective liquidus in a solidifying magma chamber: a fluid dynamic investigation. Nature 339: 613–616

Brandeis G, Jaupart C, Allegre CJ (1984) Nucleation, crystal growth and the thermal regime of cooling magmas. J Geophys Res 89: 10161–10177

Buelt JL, Timmerman CL, Oma KH, Fitzpatrick VF, Carter JG (1987) In Situ Vitrification of transuranic wastes: an updated systems evaluation and applications assessment. PNL Internal Rep 4800 (Pacific Northwest Laboratory, Richland, Washington)

Burton JA, Prim RC, Slichter WP (1953) The distribution of solute in crystals grown from the melt, part 1. Theoretical. J Chem Phys 21: 1987–1991

Cashman KV (1992) Groundmass crystallization of Mount St. Helens dacite, 1980–1986: a tool for interpreting shallow magmatic processes. Contrib Mineral Petrol 109: 431–449

Cashman KV (1993) Relationship between plagioclase crystallization and cooling rate in basaltic melts. Contrib Mineral Petrol 113: 126–142

Cashman KV, Marsh BD (1988) Crystal size distributions (CSD) in rocks and the kinetics and dynamics of crystallization II. Makaopuhi lava lake. Contrib Mineral Petrol 99: 292–305

Deer WA, Howie RA, Zussman J (1994) An introduction to the rock forming minerals. Longman, London

Dowty E (1980) Crystal growth and nucleation theory and the numerical simulation of igneous crystallization. In: Hargraves RB (ed) Physics of magmatic processes. Princeton University Press, Princeton, N.J.

Dunbar NW, Riciputi LR, Jacobs GK, Naney MT (1993) Generation of rhyolitic melt in an artificial magma: implications for fractional crystallization process in natural magmas. J Volcanol Geotherm Res 57: 157–166

Dunbar NW, Cashman KV, Dupre R (1994) Crystallization processes of anorthoclase phenocrysts in the Mount Erebus magmatic system: evidence from crystal composition, crystal size distributions and volatile contents of melt inclusions. In: Kyle PR (ed) Volcanological studies of Mount Erebus, 1st edn. American Geophysical Union, Vol 66, Washington DC, p 129–146

Gamble RP, Taylor LA (1980) Crystal/liquid partitioning in augite: effects of cooling rate. Earth Plannet Sci Lett 47: 21–33

Ghiorso MS (1987) Modelling magmatic systems: thermodynamic relations. In: Carmichael ISE, Eugster HP (eds) Thermodynamic modelling of geological materials: minerals, melts and fluids (Reviews in Mineralogy, vol. 17). Mineralogical Society of America, Washington DC, pp 443–465

Ghiorso MS, Carmichael ISE (1987) Modelling magmatic systems: petrological applications. In: Carmichael ISE, Eugster HP (eds) Thermodynamic modelling of geological materials: minerals, melts and fluids (Reviews in Mineralogy, vol. 17). Mineralogical Society of America, Washington DC, pp 467–499

Grove TL, Bence AE (1977) Experimental study of pyroxene-liquid interaction in quartz-normative basalt. Proc 8th Lunar Sci Conf: 1549–1579

Hort M, Spohn T (1991) Numerical simulation of the crystallization of multicomponent melts in the thin dikes or sills 2. Effects of heterocatalytic nucleation and composition. J Geophys Res 96: 485–499

Jacobs GK, Dunbar NW, Naney MT, Williams RT (1992) In Situ Vitrification: observations of petrological processes in a man-made magmatic system. EOS, Trans Am Geophys Union 73: 401–411

Jacobs GK, Naney MT, Dunbar NW (1993) Evidence of convection in a large, artificial magma: thermal oscillations and cooling rates recorded during crystallization. Geol Soc Am Abstr Prog 25: A367

Jacobs JW, Korotev RL, Blanchard DP, Haskins LA (1977) A well-tested procedure for instrumental neutron-activation analysis of silicate rocks and minerals. Geochim Cosmochim Acta 40: 93–114

Kirkpatrick RJ (1976) Towards a kinetic model for the crystallization of magma bodies. J Geophys Res 81: 2565–2571

Korotev RL, Lindstrom DJ (1985) Interferences from fission of U-235 in INAA of rocks. Trans Am Nucl Soc 49: 177–178

Kyle PR (1977) Mineralogy and glass chemistry of recent volcanic ejecta from Mt Erebus, Ross Island, Antarctica. New Zealand J Geol Geophys 20: 1123–1146

Lange RA, Cashman KV, Navrotsky A (1991) Direct measurements of the distribution of latent heat during cyrstallization and melting of a ugandite and an olivine basalt. Geol Soc Am Abstr Prog 23: A93

Lindsley DH (1983) Pyroxene geothermometry. Am Mineral 68: 477–493

Lofgren GE (1980) Experimental studies on the dynamic crystallization of silicate melts. In: Hargrave RB (ed) Physics of magmatic processes. Princeton University Press, Princeton, N.J.

Lofgren GE (1983) Effect of heterogeneous nucleation of basaltic textures: a dynamic crystallization study. J Petrol 24: 229–255

Norish K, Chappell BW (1977) X-ray fluorescence spectrometry. In: Zussman J (ed) Physical methods in determinative mineralogy. Academic Press, San Diego, Calif.

Ryan MP, Blevins JYK (1987) The viscosity of synthetic and natural silicate melts and glasses at high temperatures and 1 bar (10^5 Pascals) pressure and higher pressures. US Geol Surv Bull 1764: 1–563

Shaw HR (1972) Viscosity of magmatic silicate liquids: an empirical method of prediction. Am J Sci 272: 870–893

Swanson SE, Fenn PM (1986) Quartz crystallization in igneous rocks. Am Mineral 71: 331–342

Winkler HGF (1947) Kristallgrosse und Abkuhlung. Heidelb Beitr Mineral Petrogr 1: 87–104